Effective elastic properties of sandwich-structured hierarchical honeycombs: An analytical solution

Omar El-Khatib [a], S. Kumar [b], Wesley J. Cantwell [c], Andreas Schiffer [a,c,*]

[a] *Department of Mechanical Engineering, Khalifa University of Science and Technology, Abu Dhabi, 127788, United Arab Emirates*
[b] *James Watt School of Engineering, University of Glasgow, Glasgow, G12 8QQ, UK*
[c] *Advanced Research and Innovation Center (ARIC), Khalifa University of Science and Technology, Abu Dhabi, 127788, United Arab Emirates*

ARTICLE INFO

ABSTRACT

Sandwich-structured honeycombs (SSHCs) are hierarchical structures comprising sandwiched cell walls and are known to exhibit enhanced mass-specific properties. Here, we present an analytical model capable of predicting the effective elastic properties of hexagonal SSHCs, employing a sandwich beam theory that accounts for the effect of thick faces and regards the core as structurally weak. The analytical solutions of the nine elastic constants are compared with the numerical predictions obtained from a finite element-based homogenization technique, and an excellent agreement is reported for a wide range of architectural parameters such as the beam size, core thickness, and angle. Overall, it is found that SSHCs outperform conventional (monolithic) honeycombs in terms of their in-plane elastic and shear moduli, reporting values up to 20 times the monolithic counterparts of identical mass. In contrast, the out-of-plane shear moduli of the SSHCs showed reductions of at least 10% as compared to the traditional monolithic honeycomb structures.

1. Introduction

Honeycomb structures, known for their advantageous mechanical and thermal characteristics, have undergone extensive research, and found application in various fields. The advancement in understanding and designing honeycomb structures, particularly in terms of their mechanical properties, has been greatly enhanced by a combination of theoretical, computational and experimental endeavours [1]. These three methodologies are often synergistically employed to offer a holistic perspective on optimizing and crafting honeycomb designs [2]. The study of a honeycomb's mechanical response is typically approached through analytical and experimental methods [3], while advances in computational tools enabled further research via numerical modelling [4] and homogenization techniques [5]. Recently, with the development of machine learning techniques, the honeycomb design can be optimized through neural-network modelling approaches [6] alongside multiscale modelling [7] for tailored properties such as stiffness, energy absorption and strength.

In practical applications, the manufacturability of the unit cell's topology plays a crucial role in determining its design. Recent advances in additive manufacturing (AM) technologies alleviated the constraints imposed by traditional manufacturing methods, and consequently, allowed for the emergence of novel honeycomb designs with complex architectural configurations [8]. Emerging 3D printing and AM techniques have facilitated the fabrication of intricate and custom honeycomb structures across multiple length scales [9,10]. This technological progress has unlocked new avenues for realizing highly specialized designs across diverse applications [11]. Optimized honeycombs, featuring specific architectural configurations and constituent material properties, deliver superior performance metrics, including weight-specific stiffness, strength, energy absorption, and impact resistance [12]. These advancements have elevated honeycombs to a prominent status within a wide spectrum of sectors, including aerospace [13], automotive [14], and biomedical engineering [15,16].

The architectural configuration of honeycombs encompasses the manipulation of cell attributes, including cell size, shape, and arrangement, to attain precise mechanical and thermal properties. Variations in these cell parameters result in alterations in the relative density (the solid volume fraction) of honeycombs, thereby exerting a substantial influence on the honeycomb's performance. Novel honeycomb designs are realized by manipulating the unit cell designs with the intention of enhancing one or more properties. These design variations can be classified into three categories based on the implemented approach: hybrid, graded, and hierarchical honeycombs [8,11].

Hybridization of honeycombs refers to the combination of different honeycomb structures with different unit cell topologies or materials to create a hybrid structure that harnesses the advantages of each unit cell or material. Hybrid honeycombs can involve a combination of various cell shapes, sizes, or configurations within a single honeycomb structure. For example, combining the re-entrant honeycomb unit cell with a regular [17], rhombic [18] and chiral honeycomb unit cells enhanced the performance compared to the single unit cell honeycomb. Alternatively, they can combine honeycomb structures made from different materials or with distinct properties [19]. Graded honeycombs, on the other hand, are honeycomb structures in which the properties, such as cell size, wall thickness, or material composition, vary gradually or systematically across the structure. This gradient in properties can be either continuous or stepwise. For instance, the implementation of a suitable wall thickness gradient in the out-of-plane direction has been proven effective in mitigating catastrophic collapse modes, resulting in enhanced energy absorption capacity [2,20,21].

Hierarchical honeycombs are lattice structures featuring a multi-level or nested arrangement of cells in their architecture. These cells exhibit varying sizes, shapes, or structural attributes and are systematically organized in a hierarchical fashion, with smaller cells nested within larger ones. In this hierarchical design, the honeycomb structure comprises unit cells of different sizes, with the smaller ones positioned at the vertices or cell walls of the larger unit cells. This hierarchy is termed "self-similar" when both unit cells share the same topology; otherwise, it is considered "non-self-similar." Research by Zhang et al. [22] and Tan et al. [23] has demonstrated that both self-similar and non-self-similar hierarchical configurations enhance stiffness and energy absorption in comparison to the original unit cell. Moreover, Li et al. [24] have reported that the implementation of hierarchical design in sandwich panels can lead to increased bending strength.

An alternative method to realize a hierarchical honeycomb design involves the use of sandwich beams to construct cell walls, as opposed to solid beams. Fig. 1 provides a visual representation of the SSHC unit cell within a lattice structure. Because honeycombs are typically structures that are prone to bending [25], their stiffness is primarily determined by the bending stiffness of the cell walls. This stiffness can be significantly enhanced by employing the sandwich effect [26]. The use of sandwich beams involves the incorporation of lightweight core materials in the central region, resulting in a redistribution of mass towards the outer surfaces. This, in turn, leads to an increase in mass-specific stiffness [27]. Consequently, for a given relative density, it is anticipated that a sandwich-structured honeycomb (SSHC) will exhibit superior elastic stiffness compared to its monolithic honeycomb (MHC) counterpart. The earliest documentation of this concept can be traced back to Bhat et al. [28], who referred to it as "micro-sandwiching" in cellular solids. In a related study, they introduced principles for the design of "micro-sandwich honeycombs", covering their properties and fabrication techniques [29]. In essence, SSHCs share conceptual similarities with micro-sandwich honeycombs but are implemented on a larger scale.
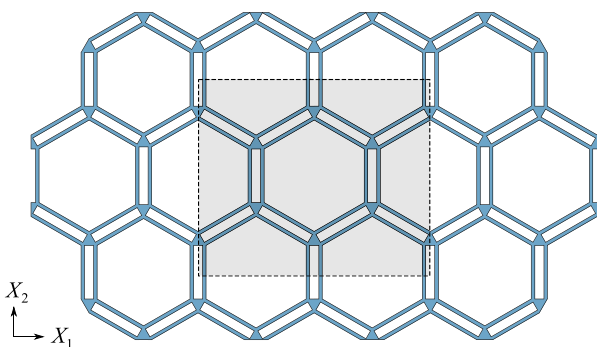

Fig. 1. Schematic of a periodic SSHC with a unit cell bounded by the dashed box. White areas represent core material, and the remainder is face material.

Additionally, Huang et al. [30] conducted a study modeling the elastic properties of hexagonal and square micro-sandwich honeycombs, revealing a significant increase in structural efficiency compared to solid beam counterparts when optimal design parameters are employed. To the best of our knowledge, there have been no reports of micro-sandwich honeycombs in other sources.

In contrast, recently, there has been a growing emphasis on large-scale sandwich-structured honeycombs. Fan et al. [31] conducted an analytical investigation into the impact of sandwich structuring in an isogrid honeycomb, while Yi et al. [32] carried out numerical analyses. Their studies revealed a significant increase in collapse load and fracture toughness. Likewise, Zhao et al. [33] and Wang et al. [34] observed a substantial improvement in specific energy absorption in the Kagome honeycomb when sandwich-structured walls were incorporated. Lastly, Usta et al. [35] demonstrated that slotted wall regular and re-entrant honeycombs achieved a higher compressive modulus through numerical simulations, which were corroborated by experimental results.

Studies involving honeycombs incorporating sandwich-structured walls have demonstrated significant promise for enhancing performance, underscoring the importance of further exploration in this field. Although certain studies have concentrated on specific design aspects, there has been limited attention directed towards fully exploring the design potential of sandwich-structured cell walls, particularly in cases where the unit cell design remains unclear. Additionally, the majority of investigations have leaned heavily on experimental or numerical methods, often neglecting systematic and in-depth analytical modelling of mechanical responses. Notwithstanding these constraints, the combined results consistently highlight improved mechanical properties when contrasted with traditional honeycomb designs.

To bridge this knowledge gap, our study is centred on the unit cell design of SSHC and a thorough examination of their elastic response. Predicting the elastic properties of sandwich-structured honeycombs is crucial for understanding their mechanical behavior, especially as current models primarily apply to conventional honeycomb designs. We introduce an analytical model rooted in sandwich beam theory, specifically incorporating thick-faced sandwich beams, and validate it through numerical simulations across a diverse range of unit cell designs. Through the incorporation of the sandwich effect into this model, our objective is to provide a comprehensive understanding of how various design parameters influence the elastic properties of SSHCs. This, in turn, facilitates the identification of optimal design configurations to maximize performance. The analytical model's predictive capabilities, coupled with numerical validation, establish a robust foundation for exploring the mechanical characteristics of sandwich-structured honeycombs, offering the potential for their efficient utilization in practical engineering applications.

2. Analytical model

Analytical formulations for predicting the elastic response of periodic 2D regular honeycombs are based on beam theory to describe the flexural stiffness of the beams constituting the unit cell geometry. The type of beam theory involved controls the accuracy of the analytical formulation. One of the earliest models presented in the literature is the Gibson–Ashby (GA) model [36], which employs classical beam theory for determining closed-form expressions for the nine elastic constants. This model can predict the elastic constants accurately for a small range of relative densities, since the inclined beams dominate the unit cell deformation over this range. However, at higher relative densities, the vertical beams and nodal areas contribute greatly to the unit cell deformation, and the GA model becomes roughly accurate at higher relative densities.

The Malek-Gibson (MG) model [37] is a more accurate version of the GA model and takes a close form to the latter. It employs a similar kinematics framework with a comprehensive inclusion of deformation modes for both inclined and vertical beams, mainly derived from

Timoshenko beam theory [38]. This model also accounts for the effect of the nodal areas in the analysis for in-plane and out-of-plane loading, since their effect becomes prominent at higher relative densities. The model exhibits accuracy as well as flexibility with regards to unit cell geometry and beam material. It was proven accurate in the cases of asymmetric hexagonal honeycombs such as a 45° angle honeycomb and a non-uniform length honeycomb. In terms of material selection, the model is applicable for beams composed of isotropic, transversely isotropic or orthotropic materials. The MG model is not applicable for SSHCs, as it was formulated for honeycombs consisting of solid beams, which will be referred to as monolithic honeycombs (MHC) in the following.

However, the kinematic framework presented in the MG model is applicable to any hexagonal honeycomb, and this provides a basis to formulate a similar model suitable for predicting the effective elastic properties of hexagonal SSHCs. In fact, both conventional honeycombs and SSHCs possess the same material symmetry and belong to the family of orthotropic materials. Their elasticity matrix consists of nine elastic constants: three elastic moduli $\{E_1^*, E_2^*, E_3^*\}$ three shear moduli $\{G_{12}^*, G_{23}^*, G_{13}^*\}$ and three Poisson's ratios $\{\nu_{12}^*, \nu_{23}^*, \nu_{13}^*\}$. In the following sections, we derive the effective elastic constants of SSHCs by integrating sandwich beam theory into the kinematic framework of the MG model.

2.1. SSHC unit cell

As shown in Fig. 2, the SSHC unit cell considered herein consists of eight inclined and four vertical sandwich beams along with six nodal areas at the intersections. For the sake of simplicity, the SSHC is assumed to be of unit width, B. For a regular honeycomb composed of a hexagonal arrangement of monolithic beams with equal length, the elastic response is determined by the thickness and configuration of the beams (length L, thickness H, angle θ) and the elastic modulus of the parent solid material, E_s. Integrating the sandwich beam geometry into the honeycomb unit cell design, the elastic response becomes a function of additional parameters namely the face sheet thickness and core thickness, denoted by t_f and t_c, respectively, and the elastic moduli of the faces E_f and added core material E_c. Thus, the response of the SSHC unit cell is controlled by six parameters: $(L, H, \theta, t_c, E_f, E_c)$. The additional parameters broaden the range of possible unit cell designs in terms of beam geometry and material pairings that grant this honeycomb design a great level of tunability. This paper focuses on hexagonal SSHCs composed of beams of equal length and arranged with varying angles θ.

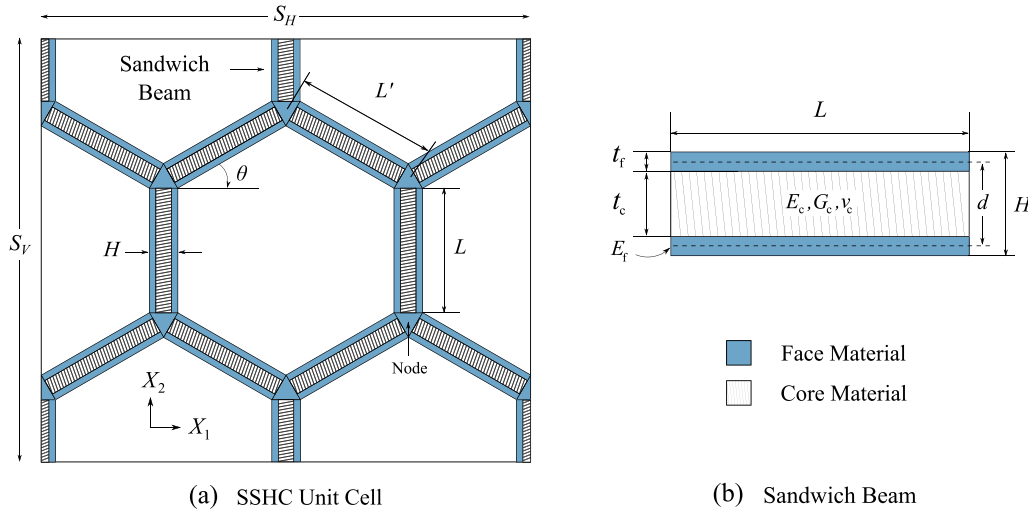For simplicity, the SSHC geometry can be defined by dimensionless parameters:

$$\overline{H} = \frac{H}{L}, \quad \overline{t}_c = \frac{t_c}{H} \tag{1}$$

where $\overline{H}$ and $\overline{t}_c$ represent the beam height-to-length ratio and the normalized core thickness, respectively. The normalized face thickness can be expressed as $\overline{t}_f = 2t_f/H = 1 - \overline{t}_c$.

The nodal area connecting the angled and vertical beams is comprised of a large triangle (N) lying between two smaller symmetric triangles (n) [37], as sketched in Fig. 3. The large triangle has a base H and height h_N:

$$h_N = H\left(\frac{2 - \sin\theta}{2\cos\theta}\right) \tag{2}$$

and the adjacent triangles have a height H and base length l_n:

$$l_n = H\left(\frac{2\sin\theta - 1}{2\cos\theta}\right) \tag{3}$$

Note that the two small triangles vanish at an angle $\theta = 30°$. From Fig. 2a the horizontal and vertical boundaries of the unit cell can be expressed as

$$S_H = 4\left[(L + l_n)\cos\theta + \frac{H}{2}\right] \tag{4}$$

$$S_V = 2[(L + l_n)\sin\theta + L + h_N] \tag{5}$$

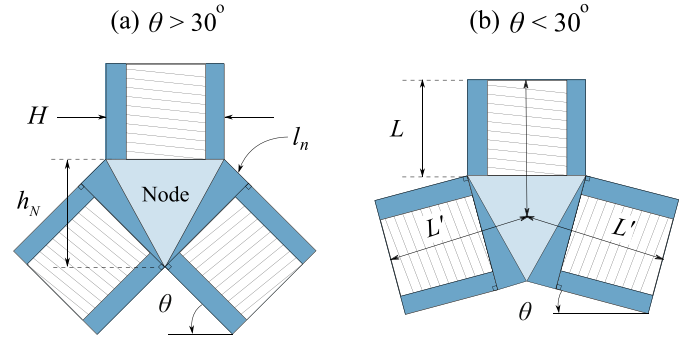Additionally, the length connecting two node centers (see Fig. 2a) in

Fig. 3. Sketch of the nodal area showing the center nodal triangle N and the smaller adjacent triangles n configuration for a honeycomb with $\theta > 30°$ (a) and $\theta < 30°$ (b).

(a) SSHC Unit Cell

(b) Sandwich Beam

Fig. 2. Schematic of the SSHC showing the major dimensions of the (a) unit cell and its (b) sandwich-structured walls.

the honeycomb is expressed as

$$L' = L + \frac{H}{2\cos\theta} \tag{6}$$

The relative density of the prismatic SSHC unit cell can be expressed in terms of a fraction of the face material density and area:

$$\overline{\rho}_{SSHC} = \left(\frac{\rho^*}{\rho_f}\right) = \frac{(\rho_c/\rho_f)3Lt_c + 3Lt_f + 2A_n + A_N}{S_V S_H} \tag{7}$$

where $A_N = Hh_N/2$ and $A_n = Hl_n/2$ are the areas of the small and large triangles, respectively (see Fig. 3). It is seen from Eq. (7) that the relative density of the SSHC not only depends on the honeycomb geometry but also on the material density ratio ρ_c/ρ_f. Analogous to conventional honeycombs, the elastic response of the SSHC is controlled by the bending and shearing deformations induced in the cell walls which can be described using sandwich beam theory discussed next.

2.2. Sandwich beam deformations

Sandwich beam theory is a type of beam theory that accounts for transverse shear deformations that occur primarily in the core of the sandwich even in case of high slenderness [39]. Hence, the total deflection $\delta(x)$ at position x on the sandwich beam can be written as

$$\delta(x) = \delta_b(x) + \delta_s(x) \tag{8}$$

where δ_b and δ_s denote the bending and shear deformations, respectively. These partial deflections are typically expressed as functions of the bending stiffness D and shear stiffness S of the sandwich. For a sandwich beam of unit thickness B, the bending stiffness D is given by [40]:

$$D = 2D_f + D_o + D_c = \frac{E_f t_f^3}{6} + \frac{E_f t_f d^2}{2} + \frac{E_c t_c^3}{12} \tag{9}$$

where $d = t_c + t_f$ is the distance separating the faces' centerlines (see Fig. 2b), while D_f and D_c are the flexural rigidities about the individual neutral axes of the faces and core, respectively. The D_o term represents the flexural stiffness of the faces due to bending about the centerline of the entire sandwich and is obtained through the parallel axis theorem. Note that Eq. (9) is applicable for the case of symmetric faces only. According to [39], the shear stiffness of a sandwich beam (unit thickness B) can be expressed as

$$S = \frac{G_c d^2}{t_c} \tag{10}$$

Standard sandwich beam theory assumes that the faces are thin, $t_f \ll t_c$, and that the core is weak, $E_c \ll E_f$, which ensures simple solutions to standard sandwich beam problems found in many engineering applications. The core is considered weak, if its flexural rigidity D_c is 1% of D_o [39]. However, sandwich beams in the SSHC can be thick-faced and less slender than generic sandwich beams, due to the size constraints imposed by the honeycomb design. Hence, it is essential to formulate the SSHC model to accommodate a broad range of sandwich beam designs for enhanced tunability of the properties of SSHCs. Assuming that the faces attain a relatively larger shear stiffness than the core, the shear deformations in the faces can be neglected. Accordingly, a solution for a thick-faced sandwich beam can be obtained by solving the differential equations:

$$\frac{d^2T}{dx^2} - b^2T = -b^2T_{tot} \tag{11}$$

$$\frac{d\delta_s}{dx} = \frac{T}{S} \tag{12}$$

where b is a constant defined as

$$b^2 = \frac{S}{2D_f} \tag{13}$$

Here, T_{tot} denotes the shear force carried by the two faces and the core, while T represents the shear force carried by the core alone.

For a hexagonal honeycomb subject to in-plane loading, equilibrium dictates that the shear force across the inclined cell walls (or beams) is constant, $T_{tot} = $ const., thus yielding a linear bending moment distribution with maximum bending moments induced at the nodal points. As sketched in Fig. 4, the antisymmetric deflection profile of the inclined beams in the honeycomb can be described by the bending deformation of two cantilever beams in series, each of length $L/2$ and loaded by a tip force $P = T_{tot}$. Taking each cantilever as a thick-faced sandwich beam, Eqs. (11)–(12) can be solved for the shear deformations $\delta_s(x)$ using appropriate boundary conditions: $T(0) = 0$, $T(L/2) = P$ and $\delta_s(0) = 0$. The solution is [39]:

$$\delta_s(x) = \frac{P}{S}\left[\frac{1}{b}\cdot\frac{e^{b(x-L)} + e^{-bx} - e^{-bL} - 1}{1 - e^{-bL}} + x\right] \tag{14}$$

With the help of Eq. (14), the bending deformations δ_b can now be obtained by solving

$$-D\frac{d^3\delta_b}{dx^3} = S\frac{d\delta_s}{dx} = T \tag{15}$$

with respect to the boundary conditions

$$\frac{d\delta_b}{dx}\bigg|_{x=0} = 0, \; \delta_b(0) = 0, \; M(L) = 0 \tag{16}$$

where the total bending moment is given by

$$M = -D\frac{d^2\delta_b}{dx^2} - 2D_f\frac{d^2\delta_s}{dx^2}. \tag{17}$$

The resulting bending deflection becomes:

$$\delta_b(x) = \frac{P}{D}\left[\frac{1}{b^3}\cdot\frac{e^{-bL} + 1 - e^{b(x-L)} - e^{-bx}}{1 - e^{-bL}} - \frac{x^3}{6} + \frac{Lx^2}{4} - \frac{x}{b^2}\right] \tag{18}$$

The axial deformation of the sandwich can be obtained by a simple rule-of-mixture calculation which yields Eq. (19) for a sandwich beam of length L subject to an axial force N:

$$\delta_a = \frac{NL}{2(2E_f t_f + E_c t_c)} \tag{19}$$

For $t_c = 0$, the sandwich beam is reduced to a monolithic beam possessing the elastic properties of the face material. In the latter case, $b \to \infty$ and $S \to \infty$, and Eqs. (14) and (18) simplify to match the solution of classical beam theory:

$$\delta_s(x) = 0, \; \delta_b(x) = \frac{Px^2}{6(2D_f + D_0)}\left(\frac{3L}{2} - x\right) \tag{20}$$

For $t_f = 0$, the sandwich beam is reduced to a monolithic beam with elastic modulus E_c. Then, $b \to \infty$ and $D = D_c$, yielding a solution that accounts for the shear deformations:

$$\delta_s(x) = \frac{Px}{S}, \; \delta_b(x) = \frac{Px^2}{6D_c}\left(\frac{3L}{2} - x\right) \tag{21}$$

2.3. In-plane elastic constants

Suppose that the SSHC unit cell shown in Fig. 2a (of unit width) is loaded by a compressive force F_1 parallel to the X_1 direction which induces a compressive deformation δ_1. The effective elastic modulus E_1^* is obtained by dividing the normal stress induced in the X_1 direction, σ_1, with the applied strain, ε_1:
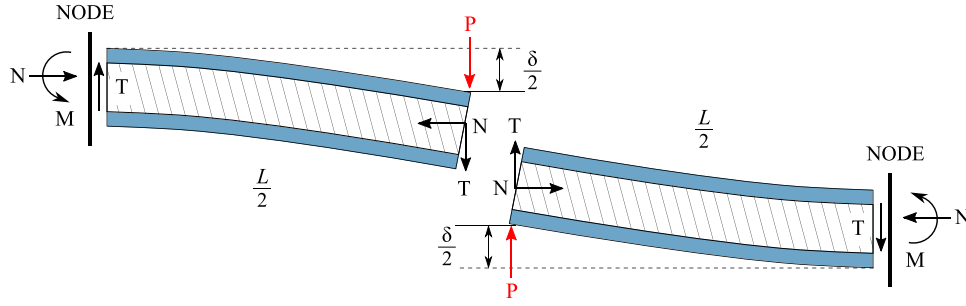
Fig. 4. Free body diagram of an inclined beam in the SSHC represented by two cantilever beams in series with equal and opposite center loads P.

$$E_1^* = \frac{\sigma_1}{\varepsilon_1} = \frac{F_1}{\delta_1} \frac{S_H}{S_V} \qquad (22)$$

Loading in the X_1 direction results in axial, bending and shearing deformations in the inclined beams of the SSHC, while the vertical beams remain undeformed. Accordingly, the total deformation δ_1 can be resolved into axial, bending and shearing deformations of the inclined beams, δ_A, δ_B, and δ_S, respectively. Since the load is transferred through four inclined beams in the unit cell, the latter relation can be written as

$$\delta_1 = 4\delta_A \cos\theta + 4(\delta_B + \delta_S)\sin\theta \qquad (23)$$

Similarly, the axial deformations of the inclined sandwich beams are twice the cantilever deformation. Using Eq. (24), we obtain the axial deflection in Eq. (28).

$$\delta_A = 2\delta_a = \frac{F_1 L \cos\theta}{2(2E_f t_f + E_c t_c)} \qquad (28)$$

By substituting Eqs. (23), (26)–(28) into Eq. (22), the final expression for the effective elastic constant E_1^* is:

$$E_1^* = \frac{S_H}{4S_V \sin^2\theta}\left[\frac{L\cot^2\theta}{2(2E_f t_f + E_c t_c)} + \frac{(e^{-bL/2}-1)^2}{1-e^{-bL}}\left(\frac{1}{Db^3} - \frac{1}{Sb}\right) + \frac{L^3}{24D} + \frac{L}{2}\left(\frac{1}{S} - \frac{1}{2Db^2}\right)\right]^{-1} \qquad (29)$$

Note that Eq. (23) assumes that all deformation occur in the cell walls of the honeycomb.

With reference to Fig. 4, the axial and transverse forces induced at the nodal points of the inclined sandwich beams are functions of the applied force F_1 and angle θ:

$$N = \frac{F_1}{2}\cos\theta \qquad (24)$$

Along the same analysis, the effective Poisson's ratios ν_{12}^* can be calculated:

$$\nu_{12}^* = -\frac{\varepsilon_{22}}{\varepsilon_{11}} = -\frac{\delta_2}{\delta_1}\frac{S_H}{S_V} \qquad (30)$$

where δ_1 is defined in Eq. (23) and $\delta_2 = -2\delta_A \sin\theta + 2(\delta_B + \delta_S)\cos\theta$. Combining the latter equations with Eqs. (26)-(28) and Eq. (30) yields:

$$\nu_{12}^* = \frac{S_H}{S_V}\frac{\sin 2\theta}{4\sin^2\theta}\left[\frac{L\cot^2\theta}{2(2E_f t_f + E_c t_c)} + \frac{(e^{-bL/2}-1)^2}{1-e^{-bL}}\left(\frac{1}{Db^3} - \frac{1}{Sb}\right) + \frac{L^3}{24D} + \frac{L}{2}\left(\frac{1}{S} - \frac{1}{2Db^2}\right)\right]^{-1} \times$$
$$\left[\frac{-L/2}{2E_f t_f + E_c t_c} + \frac{(e^{-bL/2}-1)^2}{1-e^{-bL}}\left(\frac{1}{Db^3} - \frac{1}{Sb}\right) + \frac{L^3}{24D} + \frac{L}{2}\left(\frac{1}{S} - \frac{1}{2Db^2}\right)\right] \qquad (31)$$

$$T = \frac{F_1}{2}\sin\theta \qquad (25)$$

As shown in Fig. 4, the bending and shearing deformations of the inclined sandwich beams are twice the tip deflections of a cantilever beam of length $L/2$ and can be obtained by setting $P = T = F_1\sin\theta/2$ and $x = L/2$ in Eqs. (14) and (18):

$$\delta_B = 2\delta_b(L/2) = \frac{F_1}{D}\left[\frac{1}{b^3}\cdot\frac{e^{-bL} - 2e^{-\frac{bL}{2}} + 1}{1-e^{-bL}} + \frac{L^3}{24} - \frac{L}{2b^2}\right]\sin\theta \qquad (26)$$

$$\delta_S = 2\delta_s(L/2) = \frac{F_1}{S}\left[\frac{1}{b}\cdot\frac{2e^{-\frac{bL}{2}} - e^{-bL} - 1}{1-e^{-bL}} + \frac{L}{2}\right]\sin\theta \qquad (27)$$

Now assume that the SSHC unit cell is loaded by a force F_2 in the X_2 direction, inducing a total deformation δ_2. Continuity of the displacements in the X_2 direction dictates that

$$\delta_2 = 2\delta_A \sin\theta + 2(\delta_B + \delta_S)\cos\theta + 2\delta_{Av} \qquad (32)$$

where δ_{Av} is the axial displacement induced in a vertical beam of the SSHC unit cell carrying a force $F_2/2$:

$$\delta_{Av} = \frac{F_2 L}{2(2E_f t_f + E_c t_c)} \qquad (33)$$

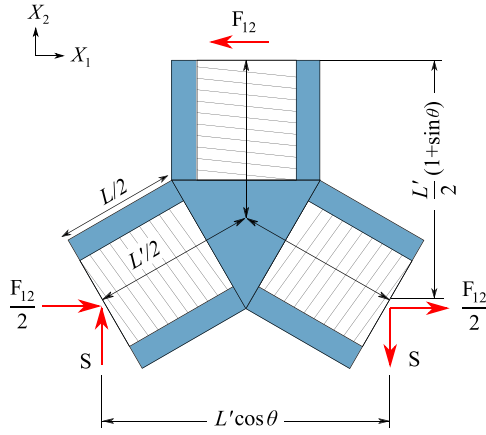The axial and shear forces in the inclined beams are now given by

Fig. 5. Free body diagram of the SSHC unit cell considered for the in-plane shear loading case.

$$N = \frac{F_2}{4}\sin\theta, \quad T = \frac{F_2}{4}\cos\theta. \tag{34}$$

Following the same procedure as for E_1^*, the effective elastic constant E_2^* is obtained as:

$$E_2^* = \frac{F_2 S_V}{\delta_2 S_H} = \frac{S_V}{S_H \cos^2\theta}\left[\frac{L\tan^2\theta}{2\left(2E_f t_f + E_c t_c\right)} + \frac{\left(e^{-bL/2}-1\right)^2}{1-e^{-bL}}\left(\frac{1}{Db^3}-\frac{1}{Sb}\right) + \frac{L^3}{24D} + \right.$$
$$\left. + \frac{L}{2}\left(\frac{1}{S}-\frac{1}{2Db^2}\right) + \frac{L}{\left(2E_f t_f + E_c t_c\right)\cos^2\theta}\right]^{-1} \tag{35}$$

The effective Poisson's ratio ν_{21}^* is defined as

$$\nu_{21}^* = -\frac{\varepsilon_{11}}{\varepsilon_{22}} = -\frac{\delta_1}{\delta_2}\frac{S_V}{S_H} \tag{36}$$

where δ_2 is given in Eq. (32) and $\delta_1 = -4\delta_A\cos\theta + 4(\delta_B + \delta_S)\sin\theta$. With the latter equations, ν_{21}^* can be written in expanded form:

$$\nu_{21}^* = \frac{S_V}{S_H}\frac{\sin 2\theta}{\cos^2\theta}\left[\frac{L\tan^2\theta}{2\left(2E_f t_f + E_c t_c\right)} + \frac{\left(e^{-bL/2}-1\right)^2}{1-e^{-bL}}\left(\frac{1}{Db^3}-\frac{1}{Sb}\right) + \frac{L^3}{24D} + \frac{L}{2}\left(\frac{1}{S}-\frac{1}{2Db^2}\right) + \right.$$
$$\left. + \frac{L/\cos\theta}{2E_f t_f + E_c t_c}\right]^{-1}\left[\frac{-L/2}{2E_f t_f + E_c t_c} + \frac{\left(e^{-bL/2}-1\right)^2}{1-e^{-bL}}\left(\frac{1}{Db^3}-\frac{1}{Sb}\right) + \frac{L^3}{24D} + \frac{L}{2}\left(\frac{1}{S}-\frac{1}{2Db^2}\right)\right] \tag{37}$$

In-plane shear loading of the SSHC by a stress τ_{12} induces a shear strain γ_{12} in the unit cell, which is the sum of the shear strain of the inclined beams γ_i and the vertical beams γ_v. To calculate the latter shear strains, it is instructive to consider the nodal area of the unit cell shown in Fig. 5.

The shear strain γ_v can be calculated from the horizontal displacement of the vertical beam δ_v, while γ_i results from the vertical displacements of the inclined beams at mid-span δ_i:

$$\gamma_v = \frac{2\delta_v}{L'(1+\sin\theta)}, \gamma_i = \frac{2\delta_i}{L'\cos\theta}. \tag{38}$$

Hence, the effective shear modulus G_{12}^* of the unit cell shown in Fig. 2 is

$$G_{12}^* = \frac{\tau_{12}}{\gamma_{12}} = \frac{F_{12}}{S_H(\gamma_i + \gamma_v)}. \tag{39}$$

where F_{12} is the shear force acting on the top face of the unit cell.

The deflection of the vertical beam consists of bending and shearing deformations, δ_{Bv} and δ_{Sv}, respectively, as well as deflections due to nodal rotations $\delta_{\phi v}$:

$$\delta_v = \delta_{\phi v} + \delta_{Bv} + \delta_{Sv} \tag{40}$$

The deflections δ_{Sv} and δ_{Bv} can be found in the same way as in the derivation of E_1^* above, but with only the deflection of a single cantilever beam considered. Hence, we set $x = L/2$ and $P = F_{12}/2$ in Eqs. (14) and (18) to obtain expressions for δ_{Sv} and δ_{Bv}, respectively. Following [25, 37], the nodal rotation ϕ can be obtained by calculating the bending deformation δ_{Bi} induced in the inclined beam by the nodal moments $M = \pm F_{12}L'/8$:

$$\phi = \frac{\delta_{Bi}}{L'} = \frac{F_{12}}{4DL'}\left[\frac{1}{b^3}\cdot\frac{e^{-bL}-2e^{-\frac{bL}{2}}+1}{1-e^{-bL}} + \frac{L^3}{24} - \frac{L}{2b^2}\right]. \tag{41}$$

The displacement due to the nodal rotation then follows as $\delta_{\phi v} = \phi L/2$ which can be substituted into Eq. (40) together with the expressions for δ_{Sv} and δ_{Bv} (not given explicitly for the sake of brevity) to obtain:

$$\delta_v = \frac{F_{12}}{2D}\left(1 + \frac{L}{4L'}\right)\left[\frac{1}{b^3}\cdot\frac{e^{-bL}-2e^{-\frac{bL}{2}}+1}{1-e^{-bL}} + \frac{L^3}{24} - \frac{L}{2b^2}\right]$$
$$+ \frac{F_{12}}{2S}\left[\frac{1}{b}\cdot\frac{e^{-bL}-2e^{-\frac{bL}{2}}+1}{1-e^{-bL}} + \frac{L}{2}\right] \tag{42}$$

The deformations of the inclined beams at mid-span, $x = L/2$, can be written as

$$\delta_i = \delta_{Ai}\sin\theta + \delta_{Si}\cos\theta \tag{43}$$

where δ_{Ai} and δ_{Si} are axial and shearing deformations that result from the shear force $T = F_{12}/4$ and axial load $N = (F_{12}/4)[\cos\theta + (1 + \sin\theta)\tan\theta]$ carried by the inclined beams (see Fig. 5).

With the help of Eqs. (14) and (19), Eq. (43) can be expressed as follows:

$$\delta_i = \frac{F_{12}L[\cos\theta + (1 + \sin\theta)\tan\theta]\sin\theta}{8\left(2E_f t_f + E_c t_c\right)} + \frac{F_{12}}{4S}\left[\frac{1}{b}\cdot\frac{e^{-bL} - 2e^{-\frac{bL}{2}} + 1}{1 - e^{-bL}} + \frac{L}{2}\right]\cos\theta.$$

(44)

The shear modulus is then computed by substituting Eqs. (38), (42) and (44) into (39):

$$G_{12}^* = \frac{L'}{S_H}\left[\left(\frac{L(\sin\theta + (1 + \sin\theta)\tan^2\theta)}{4\left(2E_f t_f + E_c t_c\right)} + \frac{1}{2S}\left(\frac{1}{b}\cdot\frac{\left(e^{-bL/2} - 1\right)^2}{1 - e^{-bL}} + \frac{L}{2}\right)\right) + \frac{1}{(1 + \sin\theta)} \times \right.$$
$$\left.\left(\frac{1}{D}\left(1 + \frac{L}{4L'}\right)\left(\frac{1}{b^3}\cdot\frac{\left(e^{-bL/2} - 1\right)^2}{1 - e^{-bL}} + \frac{L^3}{24} - \frac{L}{2b^2}\right) + \frac{1}{S}\left(\frac{1}{b}\cdot\frac{\left(e^{-bL/2} - 1\right)^2}{1 - e^{-bL}} + \frac{L}{2}\right)\right)\right]^{-1}$$

(45)

2.4. Out-of-plane constants

For loading in the X_3 direction, the cell walls of the honeycomb are subject to uniform axial stresses; hence, the constant E_3^* can be calculated using the rule of mixture where the expressions in the first and second parentheses represent the fractions of face and core material, respectively.

$$E_3^* = E_f\left(\frac{3Lt_f + 2A_e + A_d}{S_V S_H}\right) + E_c\left(\frac{3Lt_c}{S_V S_H}\right)$$

(46)

In conventional honeycombs, the effective out-of-plane Poisson's ratios, ν_{31}^* and ν_{32}^*, are equal to the Poisson's ratio of the constituent material, $\nu_{31}^* = \nu_{32}^* = \nu_s$ [37]. With the presence of sandwich beams in the honeycomb unit cell, ν_{31}^* and ν_{32}^* become functions of the Poisson's ratios of the face and core materials, ν_f and ν_c, respectively.

Now suppose that a single sandwich beam (length L, unit width B) is isolated from the SSHC and loaded in the X_3 direction, resulting in a transverse strain ε_T along the span. Equilibrium in the transverse direction dictates that:

$$2E_f t_f\left(\nu_f \varepsilon_T - \nu_{eff}\varepsilon_T\right) = E_c t_c\left(\nu_{eff}\varepsilon_T - \nu_c \varepsilon_T\right)$$

(47)

where ν_{eff} is the effective Poisson's ratio of the sandwich. Re-arranging Eq. (47) then yields:

$$\nu_{31}^* = \nu_{32}^* = \nu_{eff} = \frac{2E_f \nu_f t_f + E_c \nu_c t_c}{2E_f t_f + E_c t_c}$$

(48)

Note that setting $t_f = 0$ gives $\nu_{eff} = \nu_c$, and if $t_c = 0$ the effective Poisson's ratio becomes that of the face material. The remaining out-of-plane Poisson's ratios are obtained through the reciprocal equations:
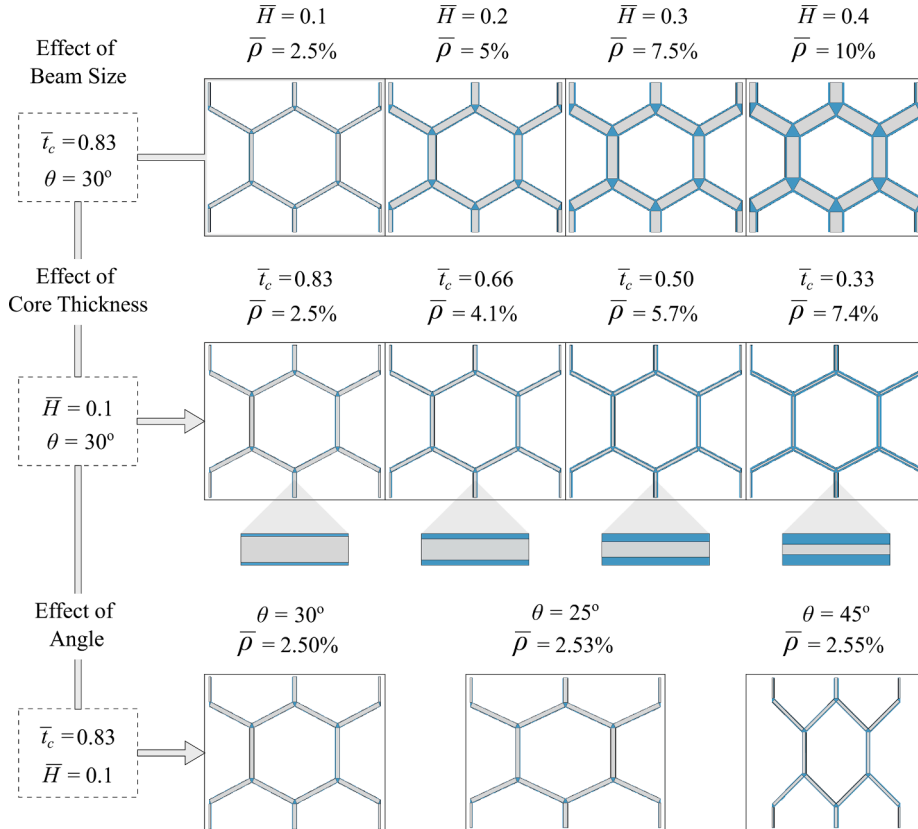

Fig. 6. Schematic of the parametric study for testing the effect of beam height-to-length ratio $\overline{H}$, core thickness $\overline{t}_c$ and angle θ. Representative geometries are given in each aspect for illustration.
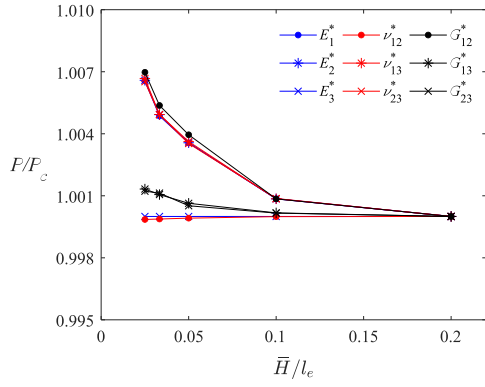
Fig. 7. Convergence of the nine effective elastic properties at different mesh sizes for a SSHC of $\overline{H}$=10%. The vertical axis shows the effective property value (P) normalized by the converged value (P_c), while the horizontal axis indicates the beam size ratio ($\overline{H}$) normalized by the element length (l_e). This plot indicated a ratio of 0.1 to generate a suitable mesh size for each of the geometries referenced in Fig. 6.

$$\nu_{13}^* = \frac{E_1^*}{E_3^*}\nu_{31}^*, \quad \nu_{23}^* = \frac{E_2^*}{E_3^*}\nu_{32}^* \tag{49}$$

Out-of-plane shear moduli for a SSHC derive exactly to match the formulation of the Malek-Gibson model [37] due to similar shear flow along the beams. The sole difference lies within the shear stress flowing in the three layers of the sandwich beam instead of one in the solid beam. This difference is translated by replacing the original shear modulus G_s with an effective shear modulus term:

$$G_{eff} = \frac{2G_f t_f + G_c t_c}{2t_f + t_c} \tag{50}$$

Thus, the out-of-plane effective shear moduli can be expressed as

follows:
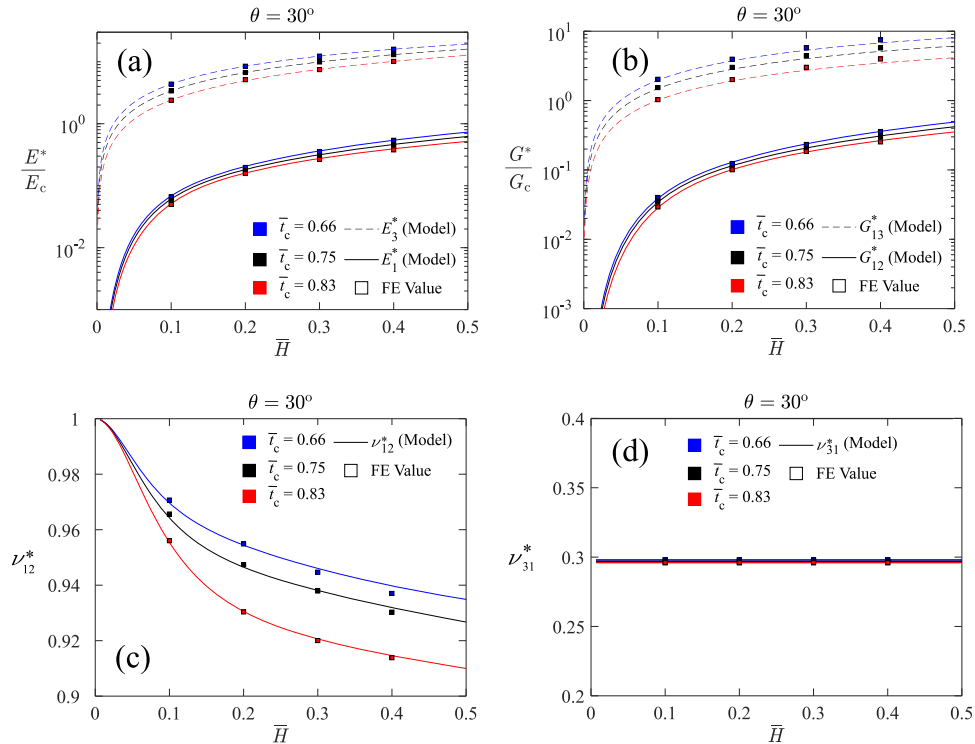
$$\frac{G_{13}^*}{G_{eff}} = \frac{H/L'}{(1+\sin\theta)\cos\theta}\left[\frac{3}{4}\frac{H}{L}\tan\theta + \frac{L}{L'}\cos^2\theta - \frac{1}{2}(2\sin\theta - 1)\cos\theta\right] \tag{51}$$

$$\frac{G_{23}^*}{G_{eff}} = \frac{H/L'}{(1+\sin\theta)\cos\theta}\left[\frac{L}{2L'} + \frac{L}{L'}\sin^2\theta - \frac{1}{2}\frac{H}{L'}\tan\theta\left(2\sin^2\theta - \sin\theta - \frac{3}{2}\right)\right] \tag{52}$$

For a detailed derivation of the latter equations, the reader is referred to Malek et al. [37].

3. Numerical model

Linear elastic finite element (FE) calculations were performed in ABAQUS/Standard (version 2019) to validate the analytical model for a wide range of SSHC designs. Herein, the unit cell shown in Fig. 2 was chosen as the representative volume element (RVE) for computational homogenization of the periodic SSHCs. The face and core materials in all RVEs were considered as isotropic and linear-elastic with constant elastic properties of $E_f = 69$ GPa and $\nu_f = 0.3$ for the faces, and $E_c = 600$ MPa and $\nu_c = 0.2$ for the cores. These values correspond to the homogenized properties of non-homogeneous materials such as metal foams and hexagonal lattices. Note that the latter selection of properties ($E_c \ll E_f$) ensured that the cores are weak compared to the faces in all RVEs.

3.1. Unit cell geometry

SolidWorks (2014) was used to develop 3D CAD models of SSHC unit cells with the design parameters $\overline{H}$, $\overline{t}_c$ and θ ranging between $0.1 \leq \overline{H} \leq 0.4$, $0.17 \leq \overline{t}_c \leq 0.95$ and $25° \leq \theta \leq 45°$, respectively. These ranges were used in a parametric study to test the validity of the model over a wide range of geometries within the design space as shown in Fig. 6. The study revolved around investigating the influence of three distinct design parameters on the elastic properties: beam height-to-
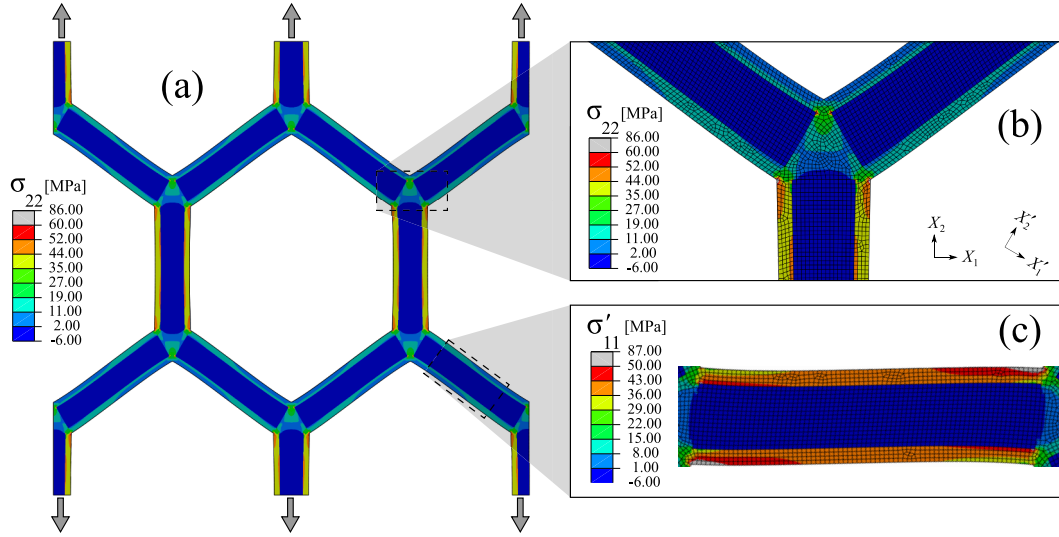

Fig. 8. Effective elastic moduli (a), effective shear moduli (b), and Poisson's ratios ν_{12}^* (c) and ν_{31}^* (d) of SSHCs as functions of $\overline{H}$ for different choices of normalized core thickness $\overline{t}_c$ and constant $\theta = 30°$; the dashed and solid lines indicate the solutions obtained from the analytical model while the colored squares represent the FE predictions for discrete data points.

Fig. 9. (a) FE contour plot of σ_{22} for loading of a SSHC with $\overline{H} = 0.3$, $\bar{t}_c = 0.75$, and $\theta = 30°$ in the X_2 direction; (b) close-up view of the σ_{22} contours in the nodal area; (c) contour plot of the axial stress σ'_{11} induced in the inclined sandwich beams with respect to the local rotated coordinates (X'_1, X'_2); all units in MPa.

length ratio $\overline{H}$, core thickness $\bar{t}_c$ and angle θ. The CAD models were imported in ABAQUS and discretized using quadratic 20-node brick elements (denoted C3D20 in ABAQUS). The fully integrated second order element is suitable for linear elastic calculations as it can accurately capture stress concentration on the surface of the honeycomb structure [41]. This feature is crucial for this study, especially that it is able to eliminate errors associated with shear-locking and hour-glassing that commonly occur in linear elements as reported in [37,42].

3.2. Boundary conditions

It has been established that the numerical solution is closest in capturing the effective elastic response of the periodic honeycomb when periodic boundary conditions (PBCs) are applied [43], and this approach was also followed herein, making use of the micromechanics plugin in ABAQUS [44]. The homogenized response of the RVE is determined through mean-field homogenization that predicts volume average stresses $\overline{\sigma}_{ij}$ defined in Eq. (53). In practice, the average stress is approximated by normalizing the sum of stresses at integration points by the current RVE volume [42]:

$$\overline{\sigma}_{ij} = \frac{1}{V} \int_V \sigma_{ij} dV \tag{53}$$

where V is the volume of the RVE.

For the case of elastic constants, the RVEs were subjected to three axial and three shear strain-driven loading scenarios, ensuring that all strains remained small ($< 5\%$). Average responses from each scenario were then fed into a post processing scheme that calculates the homogenized elastic constants $\{E_1^*, E_2^*, E_3^*, G_{12}^*, G_{23}^*, G_{13}^*, \nu_{12}^*, \nu_{23}^*, \nu_{31}^*\}$.

3.3. Solution convergence

A mesh convergence analysis was performed to ensure suitable mesh size selection for each of the SSHC geometries. The analysis indicated that the nine effective elastic constants converge when $\overline{H}/l_e > 0.1$ (see Fig. 7), where l_e is the element length (in units of length). This ratio specifies the element size required to ensure a converged solution based
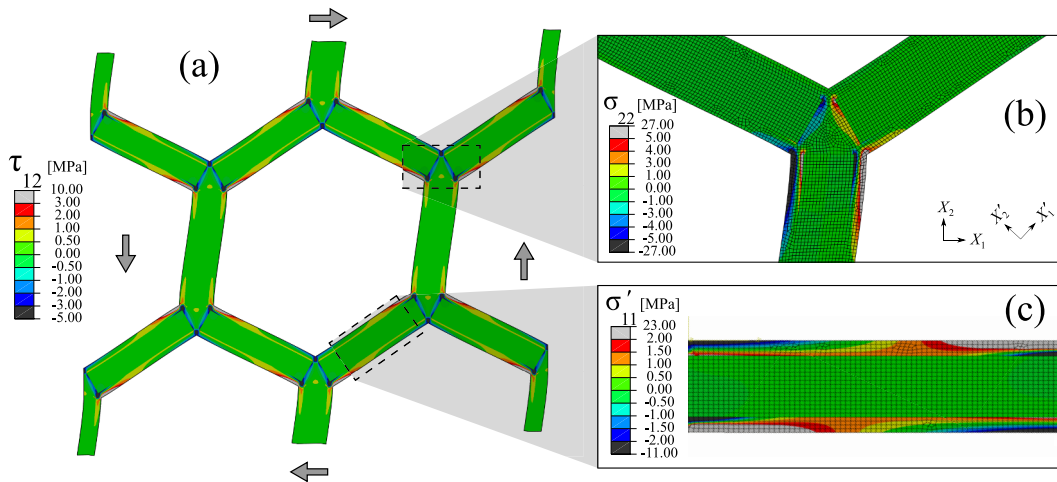

Fig. 10. (a) FE contour plot of τ_{12} for in-plane shear loading of a SSHC ($\overline{H} = 0.3$, $\bar{t}_c = 0.75$, $\theta = 30°$); (b) close-up view of the σ_{22} contours in the nodal area; (c) contour plot of the axial stress σ'_{11} induced in the inclined sandwich beams with respect to the local rotated coordinates (X'_1, X'_2); all units in MPa.

on each SSHC geometry. Accordingly, it was observed that this ratio corresponded to a minimum of four elements in the honeycomb faces. The analysis results are shown in Fig. 7 for a SSHC with $\overline{H} = 10\%$, where P is the property value normalized by the converged property value P_c.

4. Results and discussion

4.1. Analytical model validation

Fig. 8 presents the numerical and analytical predictions of the effective elastic constants as functions of $\overline{H}$ for SSHCs with $\bar{t}_c = 0.66$, 0.75, 0.83 and constant $\theta = 30°$ (see Fig. 6). Note that the predicted elastic moduli and shear moduli of the SSHCs were normalized by the core properties, E_c and G_c, respectively. At an angle of $\theta = 30°$, the predicted in-plane elastic moduli (E_1^*, E_2^*) and Poisson's ratios (ν_{12}^*, ν_{21}^*) were practically identical, as in the case of conventional monolithic honeycombs [37]; the same applies to the out-of-plane shear moduli ($G_{13}^* = G_{23}^*$) and Poisson's ratios ($\nu_{13}^* = \nu_{23}^*$). Hence, Fig. 8a–d only include the elastic constants E_1^*/E_c, E_3^*/E_c G_{12}^*/G_c, G_{13}^*/G_c, ν_{12}^* and ν_{13}^*, respectively. Overall, the analytical solutions show excellent agreement with the numerical predictions for the range of architectural parameters examined here with a difference of less than 2% from analytical solutions.

Both elastic and shear moduli in Fig. 8a and b increase with increasing beam size $\overline{H} = H/L$, which is mainly attributed to the concomitant increase in the bending and shearing stiffness of the sandwich beams. As seen in Fig. 8a, the out-of-plane elastic moduli of the SSHCs, E_3^*/E_c, were found to be almost two orders of magnitude higher than their respective in-plane moduli, E_1^*/E_c. This is expected because loading of the SSHC in the X_3 direction within the elastic regime is associated with a stiff stretch-dominated mechanism, while under in-plane loading, the stiffness of the SSHC is limited by bending and shearing of the cell walls. Similar trends were reported for the shear moduli (see Fig. 8b). Looking at the effect of the core thickness, both elastic and shear moduli were found to be inversely proportional to $\bar{t}_c$.

This effect is a consequence of the reduction in the faces thickness as the core thickness is increased, which leads to a reduction in the bending

and shearing stiffnesses of the sandwich beams, reducing the overall stiffness of the SSHC. FE contour plots in Fig. 9 support this conclusion showing the sandwich beam's faces carrying most of the applied load. Hence, increasing the face thickness would increase the load bearing capacity.

The Poisson's ratio ν_{12}^* and ν_{13}^* exhibit a non-linear relationship with increasing $\overline{H}$, as shown in Fig. 8c and d, respectively. The values of ν_{12}^* decline with higher $\overline{H}$ values, and the effect is amplified with increasing core thickness $\bar{t}_c$. However, ν_{12}^* was only weakly sensitive to the parameters $\overline{H}$ and $\bar{t}_c$, reporting variations < 10% over the parameter range shown in Fig. 8c. Moreover, ν_{12}^* tends towards unity (preserving area) as $\overline{H} \to 0$, in line with the findings of [37] for the case of monolithic honeycombs with $\theta = 30°$. The Poisson's ratio ν_{31}^* predicted by the FE model is constant with respect to $\overline{H}$ (see Fig. 8d), in line with Eq. (48), and was minutely sensitive to core thickness, as a result of $E_f \gg E_c$. It is safe to conclude that, in this range, Eq. (49) can be simplified to $\nu_{31}^* = \nu_{32}^* \approx \nu_f$.

With the presence of sandwich beam faces and core in the honeycombs, the induced stresses can attain a unique distribution which is discussed in the following. Fig. 9a illustrates the in-plane uniaxial loading of a SSHC ($\overline{H} = 0.3$, $\bar{t}_c = 0.75$, $\theta = 30°$) in the X_2 direction with close-up views of the stress fields induced in the nodal area and the inclined sandwich beams shown in Fig. 9b and c, respectively. It is clear from these figures that the load transfer takes place mainly through the faces of the sandwich beams and the nodes, due to $E_f \gg E_c$. It can also be seen that the stress fields in the faces of the vertical beams are nearly uniform (see Fig. 9a), indicating that these members deform predominantly by axial stretching. The inclined beams, on the other hand, undergo both bending and stretching, which is evident from the stress gradients in the faces along the through-thickness direction of the sandwich beam, as shown in Fig. 9c with axial stresses shown in the local rotated coordinates. A similar behavior was reported for MHCs in [37]. Moreover, the peak (axial) stresses in the inclined and vertical beams appear to be nearly identical, as seen from Fig. 9b and c. The stress contours also indicate that the cantilever beam analogy used for the inclined beams in the analytical model is appropriate (recall Fig. 4).

For the case of in-plane shear loading, Fig. 10 presents contour plots of the shear stresses τ_{12} in the global (X_1, X_2) coordinates (Fig. 10a), a
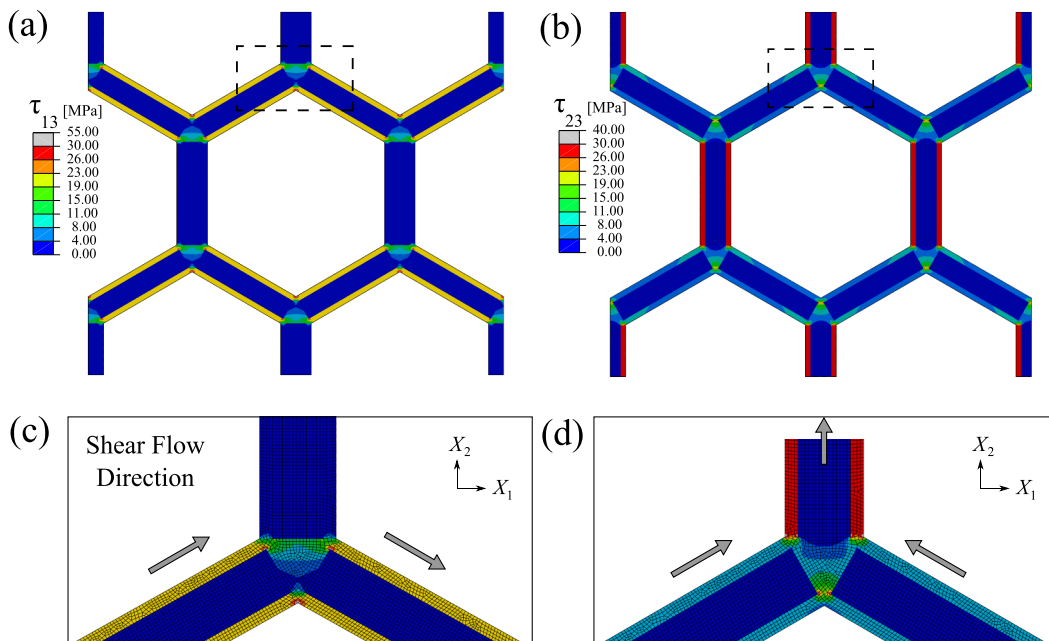

Fig. 11. FE contour plots for out-of-plane shear loading of a SSHC ($\overline{H} = 0.3$, $\bar{t}_c = 0.75$, $\theta = 30°$): (a, c) contours of τ_{13} for loading in the X_1–X_3 plane; (b, d) contours of τ_{23} for loading in the X_2 – X_3 plane.
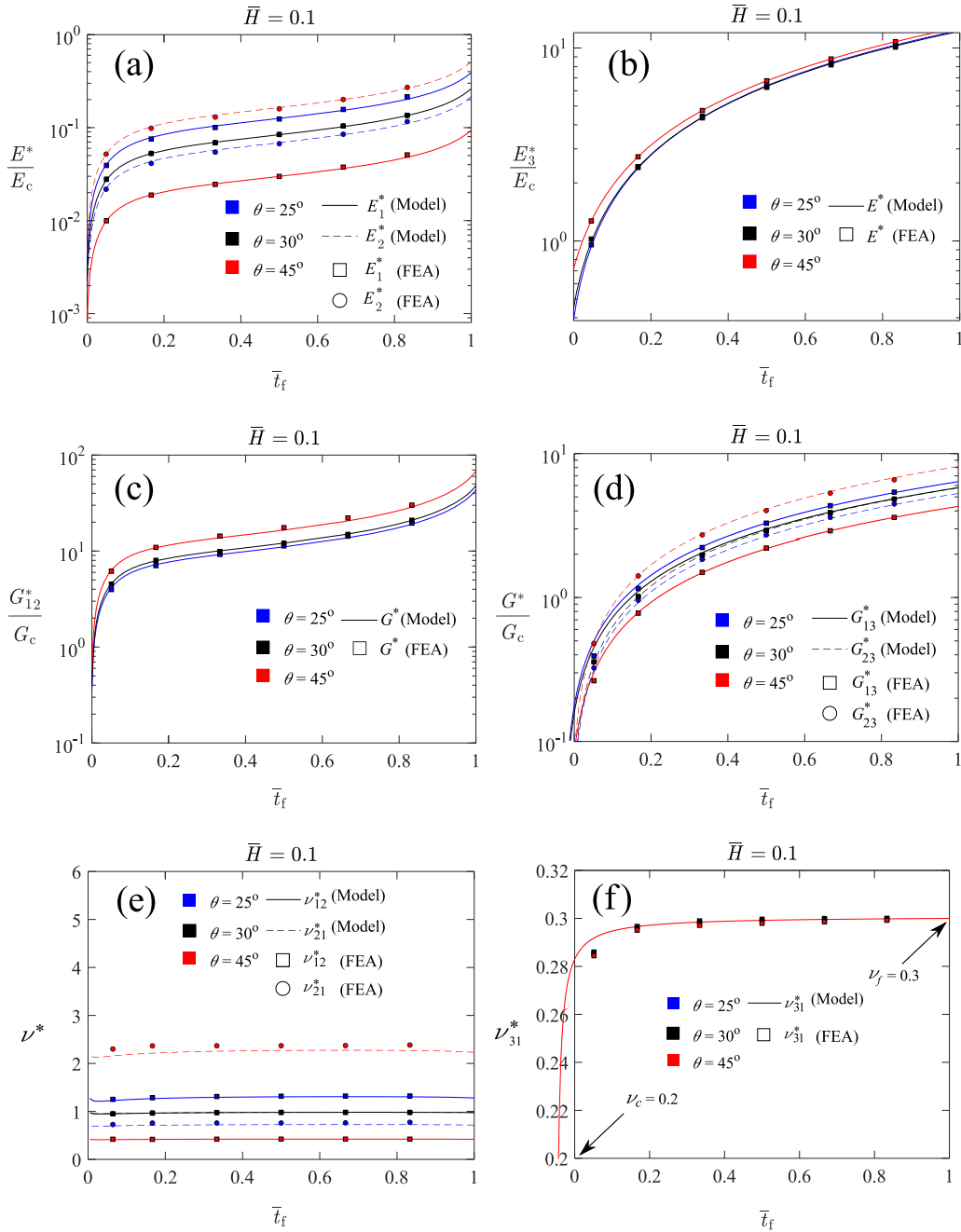
Fig. 12. Effective elastic constants of a SSHC with $\overline{H} = 0.1$, $\overline{t}_f = 0 - 1$, $\theta = 25°$, $30°$, $45°$: (a) elastic moduli (E_1^*, E_2^*), (b) elastic modulus (E_3^*), (c) shear modulus (G_{12}^*), (d) shear moduli (G_{13}^*, G_{23}^*), (e) Poisson's ratio (ν_{12}^*, ν_{21}^*) and, (f) Poisson's ratio (ν_{31}^*).

close-up view of the corresponding σ_{22} contours in the nodal region (Fig. 10b), and a contour plot of the axial stress σ_{11}' induced in an inclined sandwich beam in local (X_1', X_2') coordinates (Fig. 10c). Similar to what was observed for loading in the X_2 direction, the load transfer in the SSHC unit cell takes place primarily through the faces of the sandwich beams and two narrow strips of material within the nodes. However, the stresses in the faces are more localized near the nodes for the case of shear loading, since axial loads play only a minor role in the response of the SSHC under this type of loading. In fact, the vertical beams deform only by bending and shearing and do not experience axial forces, as seen from Fig. 10b, where the σ_{22} stress field is symmetric (in magnitude) about the mid-plane of the sandwich beam. Note that this is not the case for the inclined member shown in Fig. 10c, where the tensile surface stresses σ_{11}' are greater than the compressive ones on the

opposite face, pointing to the presence of tensile axial stresses in these members. Comparing Fig. 10b and c, the highest tensile stresses are induced in the faces of the vertical sandwich beams for the case of in-plane shear loading, and this is also applicable to MHCs, as reported in the literature [25,37].

Fig. 11a and b presents contour plots of τ_{13} and τ_{23} for out-of-plane shear loading of the SSHC in the X_1-X_3 and X_2-X_3 plane, respectively; close-ups of the τ_{13} and τ_{23} stress fields near the nodal region are also shown in Fig. 11c and d, respectively. For X_1-X_3 shear loading (see Fig. 11a), only the inclined beam faces transfer the load to adjacent beams through the connecting nodes. Small areas of stress concentrations can be observed at the outer corner of the nodes similar to what has been reported for MHCs previously [37].

For the SSHC, however, we also observe a distinct stress

concentration near the top corners of the node in Fig. 11c, due to the shear loads being transferred from the faces to the node across the sharp corners of the relatively weak sandwich cores. For shear loading in the X_2–X_3 plane, all the members of the SSHC contribute to the load transfer, as seen from Fig. 11b. However, the shear stresses in vertical beam faces are significantly higher than those induced in the inclined beam faces because, in the vertical beam, the shear loads of two inclined beams combine via load transfer through the connecting node (see Fig. 11d). Since the sandwich cores only play a minor role in the latter load transfer, they hinder the smooth flow of shear stresses through the SSHC, resulting in stress concentrations near the lower corner of the node in Fig. 11d.

Having demonstrated that the analytical model accurately predicts the elastic constants of SSHCs with constant angle $\theta = 30°$ and varying slenderness ratio $\overline{H}$, we now examine whether this is also the case for different angles θ, and a wider range of core thickness parameters $\overline{t}_c$. To this end, we plot, in Fig. 12, the analytical and FE predictions of the nine elastic constants as functions of the normalized face thickness, $\overline{t}_f = 1 - \overline{t}_c = 2t_f/H$, for different choices of angles $\theta = 25°, 30°, 45°$ and constant $\overline{H} = 0.1$. Again, the analytical calculations accurately capture the trends predicted by the FE model for all nine elastic constants of the SSHC with less than 5% difference from analytical solutions.

In line with the results presented in Fig. 8a, the elastic moduli increase in a nonlinear manner with increasing $\overline{t}_f$ (see Fig. 12a). For $0 < \overline{t}_f < 0.05$ the elastic constants E_1^*/E_c and E_2^*/E_c climb rapidly by around one order of magnitude (see Fig. 12a and b), demonstrating the significant role of the sandwich effect in stiffening the honeycomb even with very thin face thicknesses. At $\theta = 25°$ and $45°$, the in-plane elastic constants are not equivalent ($E_1^* \neq E_2^*$). In the case of E_1^*/E_c, the stiffness

of the unit cell is higher for $\theta < 30°$ and lower for $\theta > 30°$, as shown in Fig. 12a. This is expected because the inclined beams in the SSHC unit cell become more aligned with the loading direction as θ decreases, resulting in additional load to be carried by axial stretching, rather than bending and shearing. Ultimately, as $\theta \to 0°$, the beams become in line with the loading direction, and the unit cell exhibits more stretch-dominated deformation. Opposite trends are observed for E_2^*/E_c, where $\theta > 30°$ yields enhanced stiffness, as expected. Along the same reasoning, the inclined beams for $\theta > 30°$ are aligned with loading in X_2 leading to less bending and shearing deformations.

For E_3^*/E_c in Fig. 12b, the stiffness increases proportionally with face thickness $\overline{t}_f$ due to further addition of the stiffer face material to the unit cell. For instance, at $\theta = 30°$, the SSHC unit cell contains less area at the nodes since $A_n = 0$, and, according to Eq. (47), is less stiff in the X_3 direction compared to other angles. It is also observed that E_3^*/E_c is highest for $\theta = 45°$ followed by $\theta = 25°$ and $\theta = 30°$, which conforms to the area of the small triangles, A_n, within the nodes.

As shown in Fig. 12c, the in-plane shear modulus G_{12}^* complies with the same trends of the elastic modulus E_2^* discussed previously. Since the in-plane shear modulus G_{12}^* is governed by the stiffness of both inclined and vertical beams, varying the angle prompts a larger influence in terms of total deflections. In the first, the alignment of the inclined beams controls the extent of shearing, where δ_{Si} is reduced for $\theta > 30°$ similar to E_2^*. As for the vertical beams, the influence of the angle lies mostly within the deflections due to nodal rotations as $\delta_{\phi v} \propto 1/L'$. For $\theta > 30°$, the node-to-node distance L' increases (addition of small triangles n), reducing the nodal effects, and consequently, the total shear strain γ_{12}. In fact, our analytical calculations suggest that shear strains in the vertical beams are one order of magnitude larger than those of inclined
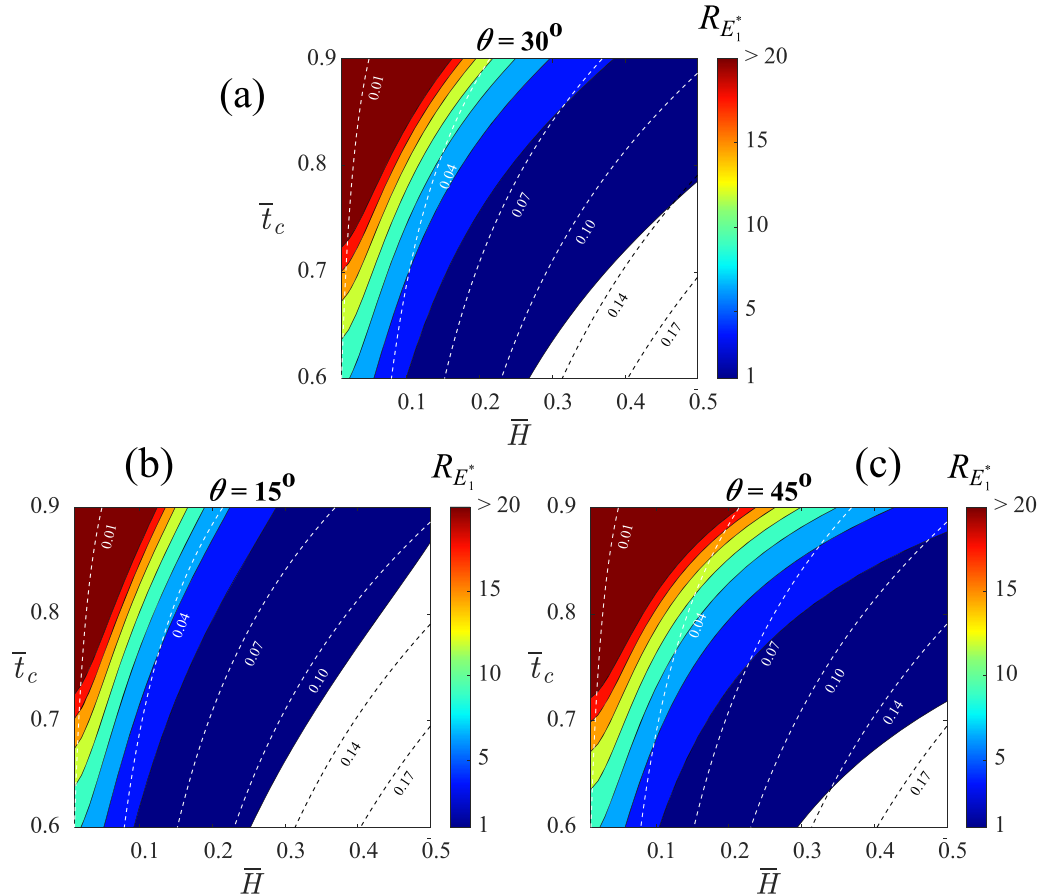

Fig. 13. Enhancemnt ratio maps of E_1^* at of a SSHC with $\overline{H} = 0 - 0.5, \overline{t}_c = 0.6 - 0.9$, and angles (a) $\theta = 30°$, (b) $\theta = 15°$, (c) $\theta = 45°$. The plots were generated for SSHCs with constant density ratio $\rho_c/\rho_f = 0.05$. The dashed lines represent contours of constant relative density of the SSHC.

beams, i.e., $\gamma_v > \gamma_i$, implying that the vertical beams carry most of the load. It is noteworthy for $\theta = 25°$ that L' is reduced compared to the other angles even when $A_n > 0$, which is a direct consequence of the nodal configuration illustrated in Fig. 3.

For the shear modulus G_{13}^*, increasing the angle yields a reduction in the stiffness (see Fig. 12d). When loading the SSHC in the X_1-X_3 plane, the shear stress τ_{13} is transferred through the inclined beams' faces and the connecting nodes solely (see Fig. 11c). Increasing the beam angle reduces its ability in effectively transferring the shear flow through its length, leading to reduced shear stiffness. With this reasoning, the additional nodal triangles aggravate this effect since they increase the length of the beam by $2l_n$. The opposite holds for lower angles.

In contrast, the shear modulus G_{23}^* is seen to increase with increasing angle θ in Fig. 12d, which is explained as follows. The shear stress τ_{23} flows through both inclined and vertical beams which alleviates full load bearing from the inclined beams, as found in [37]. This is supported by the stresses shown in Fig. 11a and b, where maximum values of 55 MPa and 40 MPa were reported for τ_{13} and τ_{23}, at $\theta = 30°$ ($l_n = 0$), respectively. Increasing the angle in this case facilitates shear flow transfer to the vertical beams as the inclined beams become relatively more upright. If the angle was reduced, the shear flow is impeded by a sharper turn from the inclined to the vertical beams causing a reduction in stiffness.

As shown in Fig. 12e, the in-plane Poisson's ratios ν_{12}^* and ν_{21}^* are (nearly) identical at $\theta = 30°$, but gradually diverge with more deviation from this angle $|\theta - 30°|$. This can be explained by recalling the reciprocal theorem, $\nu_{12}^*/\nu_{21}^* = E_1^*/E_2^*$, where the ratio E_1^*/E_2^* increases with increasing deviation of θ from $30°$, as discussed previously. For example, at $\theta = 45°$, ν_{21}^* reached a maximum of ~2.2 and ν_{12}^* a minimum of ~0.5, while at $\theta = 25°$, the change between the conjugate in-plane Poisson's ratios ranges between $0.75 - 1.25$.

As seen from the analytical predictions in Fig. 12f, the out-of-plane Poisson's ratio ν_{31}^* reaches a value of ν_c at $\bar{t}_f = 0$ and ν_f at $\bar{t}_f = 1$. Starting from $\nu_{31}^* = 0.2$, the Poisson's ratio climbs rapidly to ~95% of ν_f at only $\bar{t}_f = 0.05$. With that, most of the plotted range reads ratios close to ν_f, in line with the trends predicted by the FE model. Looking at the points 0.66, 0.75 and 0.83, the Poisson's ratio values coincide with values reported in Fig. 8d for $\bar{H} = 0.1$. Lastly, the results shown in Fig. 12f clearly indicate that ν_{31}^* is predominantly dependent on the core and face properties rather than the geometry of the honeycomb.

4.2. Enhancement ratio maps

Enhancement ratio is a measure of performance enhancement of the SSHC relative to its monolithic equivalent at a fixed relative density. It is defined as the SSHC elastic constant normalized by the corresponding

elastic constant of a MHC. For example, the enhancement ratio for E_1^* is determined by the predicted value from Eq. (29) normalized by the value predicted by the MG model for E_1^* [37]:

$$R_E = \frac{E_{1,SSHC}^*}{E_{1,MHC}^*} \tag{54}$$

If $R_E > 1$, the SSHC exhibits enhanced performance. To determine the elastic constant of the mass-equivalent MHC, its wall thickness H must be calculated to obtain the same relative density as the corresponding SSHC. This is done by identifying the height-to-length ratio $\bar{H}$ through the relative density in Eq. (8). The relative density of the MHC as function of the non-dimensional solid beam size is:

$$\bar{\rho}_{MHC} = \frac{\bar{H}^2(4 - 5\sin\theta) + 6\bar{H}\cos\theta}{4\cos^2\theta(\bar{H}^2(1 - \sin\theta) + 2\bar{H}\cos\theta + \sin\theta + 1)} \tag{55}$$

By setting the value of $\bar{\rho}_{MHC} = \bar{\rho}_{SSHC}$ and solving for $\bar{H}$ yields:

$$\bar{H}_{MHC} = -\frac{\cos\theta\left[(9 - 4\bar{\rho}_{SSHC}(\sin\theta - \cos^2\theta - 1))^{\frac{1}{2}} + 4\bar{\rho}_{SSHC}\cos^2\theta - 3\right]}{5\sin\theta + 4\bar{\rho}_{SSHC}\cos^2\theta(1 - \sin\theta) - 4} \tag{56}$$

Using Eq. (56), arbitrary solid beam dimensions L and H were obtained and plugged into the respective MG equation. Reiterating the same process for a range of SSHC relative densities, enhancement ratio maps were obtained for the elastic and shear moduli. The maps are a valuable tool for laying the foundation for SSHC design optimization by offering preliminary performance indicators for a selected set of design parameters and their impact on the elastic response. A thorough optimization analysis for the SSHC was not considered in this study.

Fig. 13 illustrates the enhancement ratio maps for E_1^* at three different honeycomb angles $\theta = 15°$, $30°$, $45°$. The ratios were computed over the range $\bar{t}_c = 60 - 90\%$ and $\bar{H} = 1 - 50\%$, since within these ranges, the SSHC model was numerically validated. Also included, in Fig. 13, are contours of relative density $\bar{\rho}$ (dashed lines) with their respective numerical values. For the SSHC, the face properties were taken as $\rho_f = 1$, $E_f = 69$ GPa, $\nu_f = 0.3$, and the properties of the core were set to $\rho_c = 0.05$, $E_c = 600$ MPa, $\nu_c = 0.2$. For the MHC, the properties of honeycomb walls were chosen equal to those of the face material in the SSHC.

The SSHC appears to increase the in-plane elastic moduli by a factor of $1 - 20$ compared to the MHC equivalent. Values higher than 20 occur for SSHCs of very slender beams with thick cores and low value of $\bar{\rho}$ (< 0.04), while values less than one occur for relatively shorter beams with thinner cores and higher $\bar{\rho}$ values (> 0.1). At $15°$ the design space for which the sandwich-structuring is beneficial (i.e. $R_E > 1$) is reduced, and the opposite is true at $45°$. This indicates that sandwich-structuring becomes more beneficial if the honeycomb walls deform
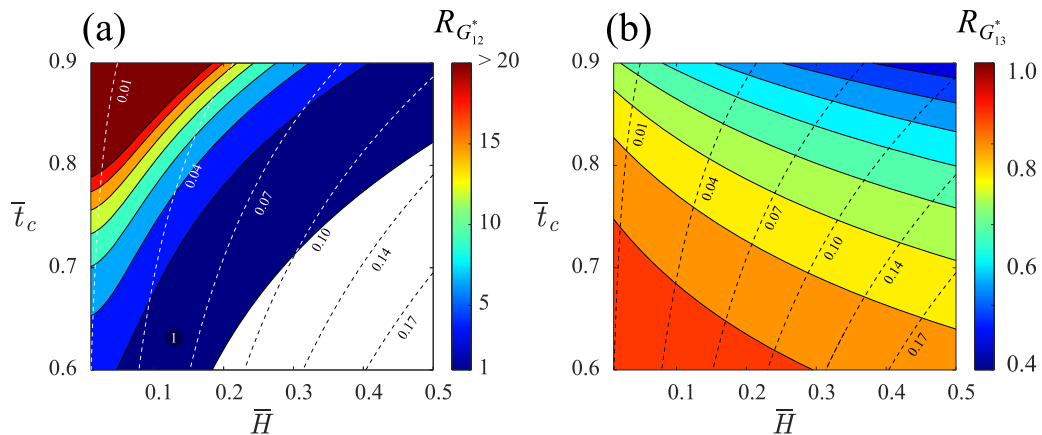

Fig. 14. Enhancement ratio maps of a SSHC with $\bar{H} = 0 - 0.5$, $\bar{t}_c = 0.6 - 0.9$, $\theta = 30°$, and $\rho_c/\rho_f = 0.05$ for (a) G_{12}^* and (b) G_{13}^*. The dashed lines represent contours of constant relative density of the SSHC.
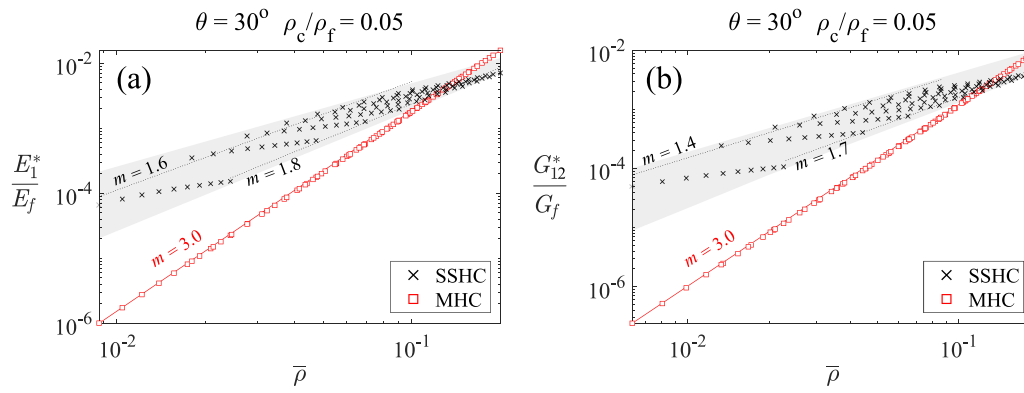
Fig. 15. Scaling of elastic constants E_1^*/E_f (a) and G_{12}^*/G_f (b) with relative densities for MHCs ($\theta = 30°$) and SSHCs ($\overline{H} = 0.1, \overline{t}_c = 0.6 - 0.9, \theta = 30°$). The plots were generated for SSHCs with $\rho_c/\rho_f = 0.05$.

predominantly by bending rather than stretching, which is the case when the angle θ increases in a SSHC loaded in the X_1 direction.

The enhancement ratios for the in-plane and out-of-plane shear moduli at $\theta = 30°$ are illustrated in Fig. 14a and b, respectively, including contours of $\overline{\rho}$ (dashed lines). It seems that the in-plane shear modulus G_{12}^* closely matches the enhancement maps of E_1^* (see Fig. 14a). For the out-of-plane shear modulus G_{13}^*, the SSHC attains a negative enhancement compared to the equivalent MHC (see Fig. 14b), where the reduction in the shear modulus ranged between 0.1 – 0.6 over the plotted range. The reduction in stiffness is more prominent for thicker beams ($\overline{H}= 40 – 50\%$) and cores ($\overline{t}_c= 80 – 90\%$). It is arguable that the sandwich beam reduces the ability to transfer the shear load to adjacent beams through the nodes. With thicker beams, the area of the node is inherently increased according to Eq. (6), and thus impedes the shear flow from one sandwich beam to the other. As a result, the beams suffer higher stresses due to the stress concentrations at the core-node interfaces, as shown in Fig. 11c and d. Unlike sandwich beams, the solid beams of a MHC allow better transfer of the load through the nodes in absence of stress concentrations. It is important to note that, since the contour lines of constant $\overline{\rho}$ are almost perpendicular to those of the enhancement ratios in Fig. 14b, the reductions in G_{13}^* can be mitigated by choosing appropriate $\{\overline{H}, \overline{t}_c\}$ combinations without affecting the relative density $\overline{\rho}$ of the designed structure.

4.3. Gibson–Ashby scaling

The analytical predictions presented in Figs. 13 and 14 were used to examine the scaling relations between the in-plane elastic moduli and the relative density of SSHCs. In Fig. 15, the normalized elastic constants E_1^*/E_f and G_{12}^*/G_f are plotted as functions of the relative density $\overline{\rho}$ for SSHCs with fixed design parameters $\overline{H}$=0.1, $\theta = 30°$ and $\rho_c /\rho_f = 0.05$; the relative density was varied by adjusting the normalized face thickness within the range $\overline{t}_f = 0.6 - 0.9$. Also included in Fig. 15 are the corresponding predictions obtained for MHCs with $\theta = 30°$, where $\overline{\rho}$ was varied by adjusting the parameter $\overline{H}$. The plots were then fitted using the Gibson–Ashby scaling law: $E^*/E_s \propto \overline{\rho}^m$ [45], where E^* is the effective property of the honeycomb, E_s is the bulk material property and m is the scaling exponent governed by the topology. The Gibson–Ashby model is most notable in predicting properties of cellular materials and periodic structures [46]. Determining the exponent allows to quantitatively compare the deformation behavior of the different honeycomb unit cells. Depending on the cell topology and loading conditions, a cellular solid can exhibit bend-dominated or stretch-dominated deformation, or a mixture of both [47]. A purely stretch-dominated structure follows a scaling exponent of $m \approx 1$, while a bend-dominated 2D structure follows $m \approx 3$.

In Fig. 15a and b, the MHC exhibits an exponent of $m = 3$, indicating

the expected purely bend-dominated behavior. In contrast, the in-plane elastic modulus of the SSHC yields $m = 1.6 - 1.8$ for $\overline{t}_c= 0.6 - 0.9$ in Fig. 15a, and $m = 1.4 - 1.7$ for the shear modulus in Fig. 15b. Hence, it is evident that the SSHC exhibits a mixed deformation behavior associated with reduced coupling between stiffness and relative density, yielding a much-improved mechanical performance at low $\overline{\rho}$ values.

4.4. Limitations and future work

The SSHC analytical model offers a powerful tool for predicting the effective elastic properties that can aid in performance investigation, conceptual design generation and optimization of these structures in terms of geometry and face/core material pairings. Nevertheless, the current model suffers from some limitations that can be resolved in future work.

Firstly, the weak core assumption narrows the design options of the core, and requires careful consideration in material type selection for the case of homogenous materials. Other core conditions and material types can be investigated in future work. The governing differential equations can be customized to derive unique deflection formulas for a desired core condition or design that generates a specialized form of the SSHC model.

Secondly, the core design in the current model concerns solid homogenous cores that exhibit isotropic material behavior. Other core designs with non-homogenous lattice structures, such as web-cores, can be explored using the current model in future work. While not verified in this study, the model is expected to provide accurate predictions by substituting isotropic core properties with the homogenized properties in the equations. Also, the analytical model can be easily adapted to other types of honeycombs, such as the square, re-entrant and Kagome honeycombs.

Additionally, the experimental investigation of the elastic response of SSHCs was challenging due to difficulties in fabricating periodic SSHC structures at a sufficiently small scale. The lack of experimental validation is a limitation in the current study and remains an important element for future research.

Another area of future work is to explore the potential of SSHCs as core materials of sandwich panels. Based on a work by Li et al. [17], where sandwich panels with hierarchical honeycomb cores were studied, sandwich structures with SSHC cores could offer higher weight-specific bending strength as compared to those involving conventional honeycomb cores. SSHCs with cellular core architectures are also expected to increase the specific energy absorption of sandwich panels due to the occurrence of multi-scale collapse processes. This feature is directly related to the crushing behavior of the cellular core between the face sheets of the SSHC that is dependent on the core material type and design [27]. Moreover, integrating SSHCs in sandwich panels allows for greater tunability of mechanical properties, making

them suitable for a wider range of engineering applications.

5. Conclusion

In this study, sandwich-structured honeycombs (SSHCs) were examined for their potential to enhance the elastic stiffness of traditional hexagonal honeycombs. An analytical model was developed to predict the effective elastic response of SSHCs composed of isotropic linear elastic face and core materials. The model is based on a sandwich beam theory that accounts for the effect of thick faces, assumes a weak core and rigid nodes.

A parametric study was conducted to investigate the sensitivity of the elastic constants to variations in the SSHC architectural parameters. The analytical solutions of the nine elastic constants were compared to numerical predictions obtained from a FE-based homogenization technique, and excellent agreement was reported with errors of less than 5%.

Enhancement ratio maps were generated to demarcate the regions in the design space for which sandwich-structuring yields enhanced elastic stiffness. Accordingly, the in-plane stiffness increases in most of the design space with pronounced enhancements at lower relative densities. However, the SSHCs showed reductions in the out-of-plane shear moduli by 10% – 60% due to stress concentrations around the core that hinder load transfer to adjacent beams.

Lastly, Gibson–Ashby scaling showed that the SSHC exhibits scaling exponents $m = 1.6 - 1.8$, that fall between those of the bend-dominated conventional honeycomb ($m = 3$) and a fully stretch-dominated lattice ($m = 1$). This indicates that the integration of sandwich walls in honeycomb structures reduces the coupling between elastic stiffness and relative density.

CRediT authorship contribution statement

Omar El-Khatib: Formal analysis, Validation, Investigation, Data curation, Visualization, Writing – original draft. **S. Kumar:** Supervision, Writing – review & editing. **Wesley J. Cantwell:** Supervision, Writing – review & editing. **Andreas Schiffer:** Conceptualization, Supervision, Writing – review & editing, Project administration, Funding acquisition.

Declaration of Competing Interest

The authors declare that they have no known competing financial interests or personal relationships that could have appeared to influence the work reported in this paper.

Data availability

Data will be made available on request.

Acknowledgments

References

[1] Fleck NA, Deshpande VS, Ashby MF. Micro-architectured materials: past, present and future. Proc R Soc A Math Phys Eng Sci 2010;466(2121):2495–516. https://doi.org/10.1098/rspa.2010.0215.

[2] Kumar S, Ubaid J, Abishera R, Schiffer A, Deshpande VS. Tunable energy absorption characteristics of architected honeycombs enabled via additive manufacturing. ACS Appl Mater Interfaces 2019;11(45):42549–60. https://doi.org/10.1021/acsami.9b12880.

[3] Karakoç A, Freund J. Experimental studies on mechanical properties of cellular structures using Nomex® honeycomb cores. Compos Struct 2012;94(6):2017–24. https://doi.org/10.1016/j.compstruct.2012.01.024.

[4] Sorohan Ş, Sandu M, Sandu A, Constantinescu DM. Finite element models used to determine the equivalent in-plane properties of honeycombs. Mater Today Proc 2016;3(4):1161–6. https://doi.org/10.1016/j.matpr.2016.03.013.

[5] Moeini M, Begon M, Lévesque M. Numerical homogenization of a linearly elastic honeycomb lattice structure and comparison with analytical and experimental results. Mech Mater 2022;167(December 2021):104210. https://doi.org/10.1016/j.mechmat.2022.104210.

[6] Karathanasopoulos N, Rodopoulos DC. Enhanced cellular materials through multiscale, variable-section inner designs: mechanical attributes and neural network modelling. Materials (Basel) 2022;15(10). https://doi.org/10.3390/ma15103581.

[7] Kochmann DM, Hopkins JB, Valdevit L. Multiscale modeling and optimization of the mechanics of hierarchical metamaterials. MRS Bull 2019;44(10):773–81. https://doi.org/10.1557/mrs.2019.228.

[8] Huang T, Gong Y, Zhao S. Effective in-plane elastic modulus of a periodic regular hexagonal honeycomb core with thick walls. J Eng Mech 2018;144(2):1–10. https://doi.org/10.1061/(asce)em.1943-7889.0001412.

[9] Xu M, Xu Z, Zhang Z, Lei H, Bai Y, Fang D. Mechanical properties and energy absorption capability of AuxHex structure under in-plane compression: theoretical and experimental studies. Int J Mech Sci 2019;159(March):43–57. https://doi.org/10.1016/j.ijmecsci.2019.05.044.

[10] Schneider J, Kumar S. Comparative performance evaluation of microarchitected lattices processed via SLS, MJ, and DLP 3D printing methods: experimental investigation and modelling. J Mater Res Technol 2023;26:7182–98. https://doi.org/10.1016/j.jmrt.2023.09.061.

[11] Qi C, Jiang F, Yang S. Advanced honeycomb designs for improving mechanical properties: a review. Compos Part B Eng 2021;227:109393. https://doi.org/10.1016/j.compositesb.2021.109393.

[12] Wang Z. Recent advances in novel metallic honeycomb structure. Compos Part B Eng 2019;166(February):731–41. https://doi.org/10.1016/j.compositesb.2019.02.011.

[13] Le VT, Ha NS, Goo NS. Advanced sandwich structures for thermal protection systems in hypersonic vehicles: a review. Compos Part B Eng 2021;226 (September):109301. https://doi.org/10.1016/j.compositesb.2021.109301.

[14] Bardhan P. Ceramic honeycomb filters and catalysts. Curr Opin Solid State Mater Sci 1997;2(5):577–83. https://doi.org/10.1016/S1359-0286(97)80048-4.

[15] Wang S, et al. Honeycomb structure is promising for the repair of human bone defects. Mater Des 2021;207:109832. https://doi.org/10.1016/j.matdes.2021.109832.

[16] Bhate D, Penick CA, Ferry LA, Lee C. Classification and selection of cellular materials in mechanical design: engineering and biomimetic approaches. Designs 2019;3(1):1–31. https://doi.org/10.3390/designs3010019.

[17] Xu M, et al. In-plane compression behavior of hybrid honeycomb metastructures: theoretical and experimental studies. Aerosp Sci Technol 2020;106:106081. https://doi.org/10.1016/j.ast.2020.106081.

[18] Fu MH, Chen Y, Hu LL. A novel auxetic honeycomb with enhanced in-plane stiffness and buckling strength. Compos Struct 2017;160(October):574–85. https://doi.org/10.1016/j.compstruct.2016.10.090.

[19] Su Y, Wu X, Shi J. A novel 3D printable multimaterial auxetic metamaterial with reinforced structure: improved stiffness and retained auxetic behavior. Mech Adv Mater Struct 2022;29(3):408–18. https://doi.org/10.1080/15376494.2020.1774690.

[20] Andrew JJ, Ubaid J, Hafeez F, Schiffer A, Kumar S. Impact performance enhancement of honeycombs through additive manufacturing-enabled geometrical tailoring. Int J Impact Eng 2019;134:103360. https://doi.org/10.1016/j.ijimpeng.2019.103360.

[21] J . JA, Schneider J, Schiffer A, Hafeez F, Kumar S. Dynamic crushing of tailored honeycombs realized via additive manufacturing. Int J Mech Sci 2022;219(August 2021):107126. https://doi.org/10.1016/j.ijmecsci.2022.107126.

[22] Zhang D, Fei Q, Liu J, Jiang D, Li Y. Crushing of vertex-based hierarchical honeycombs with triangular substructures. Thin-Walled Struct 2020;146 (September 2019):106436. https://doi.org/10.1016/j.tws.2019.106436.

[23] Tan HL, He ZC, Li KX, Li E, Cheng AG, Xu B. In-plane crashworthiness of re-entrant hierarchical honeycombs with negative Poisson's ratio. Compos Struct 2019;229 (July). https://doi.org/10.1016/j.compstruct.2019.111415.

[24] Li Z, Wang Z, Wang X, Zhou W. Bending behavior of sandwich beam with tailored hierarchical honeycomb cores. Thin-Walled Struct 2020;157(August):107001. https://doi.org/10.1016/j.tws.2020.107001.

[25] Ashby MF, Gibson LJ. Cellular solids: structure and properties. 2nd ed. Cambridge University Press; 1997.

[26] Kooistra GW, Deshpande V, Wadley HNG. Hierarchical corrugated core sandwich panel concepts. J Appl Mech Trans ASME 2007;74(2):259–68. https://doi.org/10.1115/1.2198243.

[27] Kolodziejska JA, Roper CS, Yang SS, Carter WB, Jacobsen AJ. Research Update: enabling ultra-thin lightweight structures: microsandwich structures with microlattice cores. APL Mater 2015;3(5). https://doi.org/10.1063/1.4921160.

[28] Bhat TB, O'Donnell T, Wang TG. Microsandwich cellular solids. 1989 [Online]. Available, https://ntrs.nasa.gov/citations/19910048014.

[29] Bhat TB, Wang TG, Gibson LJ. Microsandwich Honeycomb. SAMPE J 1989;25 [Online]. Available, https://ntrs.nasa.gov/citations/19890051861.

[30] Jong-Shin H, Shun-Yi H. Optimum microstructure of stiff microsandwich honeycombs. J Chin Soc Mech Eng 1994;15(3):297–302.

[31] Fan HL, Jin FN, Fang DN. Mechanical properties of hierarchical cellular materials. Part I: analysis. Compos Sci Technol 2008;68(15–16):3380–7. https://doi.org/10.1016/j.compscitech.2008.09.022.

[32] Yi T. Mechanical properties of a hierarchical honeycomb with sandwich walls. Proc Inst Mech Eng Part C J Mech Eng Sci 2016;230(16):2765–75. https://doi.org/10.1177/0954406215602284.

[33] Zhao L, Zheng Q, Fan H, Jin F. Hierarchical composite honeycombs. Mater Des 2012;40:124–9. https://doi.org/10.1016/j.matdes.2012.03.009.

[34] Wang Z, Lei Z, Li Z, Yuan K, Wang X. Mechanical reinforcement mechanism of a hierarchical Kagome honeycomb. Thin-Walled Struct 2021;167(July):108235. https://doi.org/10.1016/j.tws.2021.108235.

[35] Usta F, Scarpa F, Türkmen HS. Edgewise compression of novel hexagonal hierarchical and asymmetric unit cells honeycomb metamaterials. Mater Today Commun 2020;24(November 2019):101102. https://doi.org/10.1016/j.mtcomm.2020.101102.

[36] Gibson LJ, Ashby MF, Schajer GS, Robertson CI. The mechanics of two-dimensional cellular materials. Proc R Soc Lond A Math Phys Sci 1982;382(1782):25–42. https://doi.org/10.1098/rspa.1982.0087. Jul.

[37] Malek S, Gibson L. Effective elastic properties of periodic hexagonal honeycombs. Mech Mater 2015;91(P1):226–40. https://doi.org/10.1016/j.mechmat.2015.07.008.

[38] Timoshenko SP. On the correction for shear of the differential equation for transverse vibrations of prismatic bars. Lond Edinb Dubl Philos Mag J Sci 1921;41 (245):744–6. https://doi.org/10.1080/14786442108636264. May.

[39] Zenkert D. An introduction to sandwich construction. 1995. no. Student.

[40] Allen HG. Analysis and Design of Structural Sandwich Panels. *Analysis and design of structural sandwich panels,* first. Elsevier; 1969.

[41] Zienkiewicz OC, Taylor R. The finite element method. McGraw-Hill Book Company; 1989.

[42] Wu L, Noels L, Adam L, Doghri I. A multiscale mean-field homogenization method for fiber-reinforced composites with gradient-enhanced damage models. Comput Method Appl Mech Eng 2012;233–236:164–79. https://doi.org/10.1016/j.cma.2012.04.011.

[43] Xia Z, Zhang Y, Ellyin F. A unified periodical boundary conditions for representative volume elements of composites and applications. Int J Solid Struct 2003;40(8):1907–21. https://doi.org/10.1016/S0020-7683(03)00024-6.

[44] McLendon WR. Micromechanics plugin. 2016. p. 1–22.

[45] The mechanics of three-dimensional cellular materials. Proc R Soc Lond A Math Phys Sci 1982;382(1782):43–59. https://doi.org/10.1098/rspa.1982.0088. Jul.

[46] Maconachie T, et al. SLM lattice structures: properties, performance, applications and challenges. Mater Des 2019;183:108137. https://doi.org/10.1016/j.matdes.2019.108137.

[47] Baghous N, Barsoum I, Abu Al-Rub RK. The effect of Lode parameter on the yield surface of Schoen's IWP triply periodic minimal surface lattice. Mech Mater 2022; 175(September):104473. https://doi.org/10.1016/j.mechmat.2022.104473.